Knitting the Catalytic Pattern of Artificial Photosynthesis to a Hybrid Graphene Nanotexture

Mildred Quintana,[†] Alejandro Montellano López,[†] Stefania Rapino,[‡] Francesca Maria Toma,[†] Matteo Iurlo,[‡] Mauro Carraro,[§] Andrea Sartorel,[§] Chiara Maccato,[§] Xiaoxing Ke,[⊥] Carla Bittencourt,[⊥] Tatiana Da Ros,[†] Gustaaf Van Tendeloo,[⊥] Massimo Marcaccio,[‡] Francesco Paolucci,[‡,*] Maurizio Prato,[†,*] and Marcella Bonchio[§,*]

[†]Center of Excellence for Nanostructured Materials (CENMAT) and INSTM, unit of Trieste, Dipartimento di Scienze Chimiche e Farmaceutiche, University of Trieste, Piazzale Europa 1, I-34127 Trieste, Italy, [‡]Dipartimento di Chimica "G. Ciamician" and INSTM, unit of Bologna, University of Bologna, Via F. Selmi 2, 40126 Bologna, Italy, [§]ITM-CNR and Dipartimento di Scienze Chimiche, University of Padova, via F. Marzolo 1, 35131 Padova, Italy, and [⊥]EMAT, University of Antwerp, Groenenborgerlaan 171, B-2020 Antwerp, Belgium

ABSTRACT The artificial leaf project calls for new materials enabling multielectron catalysis with minimal overpotential, high turnover frequency, and long-term stability. Is graphene a better material than carbon nanotubes to enhance water oxidation catalysis for energy applications? Here we show that functionalized graphene with a tailored distribution of polycationic, quaternized, ammonium pendants provides an sp^2 carbon nanoplatform to anchor a totally inorganic tetraruthenate catalyst, mimicking the oxygen evolving center of natural PSII. The resulting hybrid material displays oxygen evolution at overpotential as low as 300 mV at neutral pH with negligible loss of performance after 4 h testing. This multilayer electroactive asset enhances the turnover frequency by 1 order of magnitude with respect to the isolated catalyst, and provides a definite up-grade of the carbon nanotube material, with a similar surface functionalization. Our innovation is based on a noninvasive, synthetic protocol for graphene functionalization that goes beyond the ill-defined oxidation–reduction methods, allowing a definite control of the surface properties.

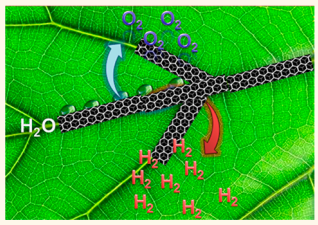

KEYWORDS: carbon nanostructures · functionalized graphene · artificial photosynthesis · water oxidation catalysis · polyoxometalates

Bioenergy is renewed daily by catalytic water splitting, taking place at the heart of the photosynthetic machinery embedded in leaves. Under artificial conditions, the same task, leading to the continuous extraction of O_2 and H_2 as solar fuels, poses a severe challenge and it represents one urgent concern of fundamental and applied energy research.[1−6] The pitfall stems from the high thermodynamic and kinetic barrier of the water oxidation stage, where electrons and protons are sequentially removed, after the light collection events. This issue calls for the design of innovative catalytic systems, mastering multielectron transfer, and enabling water oxidation at low overpotential, that is, close to the thermodynamic requirement (E^0 = 1.23 V) with increased long-term stability.[7,8]

This is one central goal of the artificial leaf project, which relies on a tailored merging of water oxidation catalysis (WOC) and nanomaterials research.[9−12] The synergy expected from these two disciplines targets the "all-around" shaping of the catalyst environment that can be tuned at the nanoscale by providing a suitable material support.[9−12] The final aim is the fabrication of nanostructured oxygen evolving anodes (OEA) operating at low overpotential and high current density for device engineering.

While carbon nanotubes have been widely used for electro-catalytic applications, and serve as WOC support outperforming amorphous materials, there is no reported instance for the use of graphene and its modification to cast molecular WOCs.[13−16] In this context, graphene offers some unique features vis-à-vis the engineering of electrodic surfaces. In detail, the graphene nanoplatform is expected to foster an excellent bidimensional charge carrier transport,[17−22] thus facilitating redox surface events and catalysis. Moreover, it

* Address correspondence to francesco.paolucci@unibo.it, prato@units.it, marcella.bonchio@unipd.it.

Received for review November 15, 2012 and accepted December 17, 2012.

Published online December 17, 2012
10.1021/nn305313q

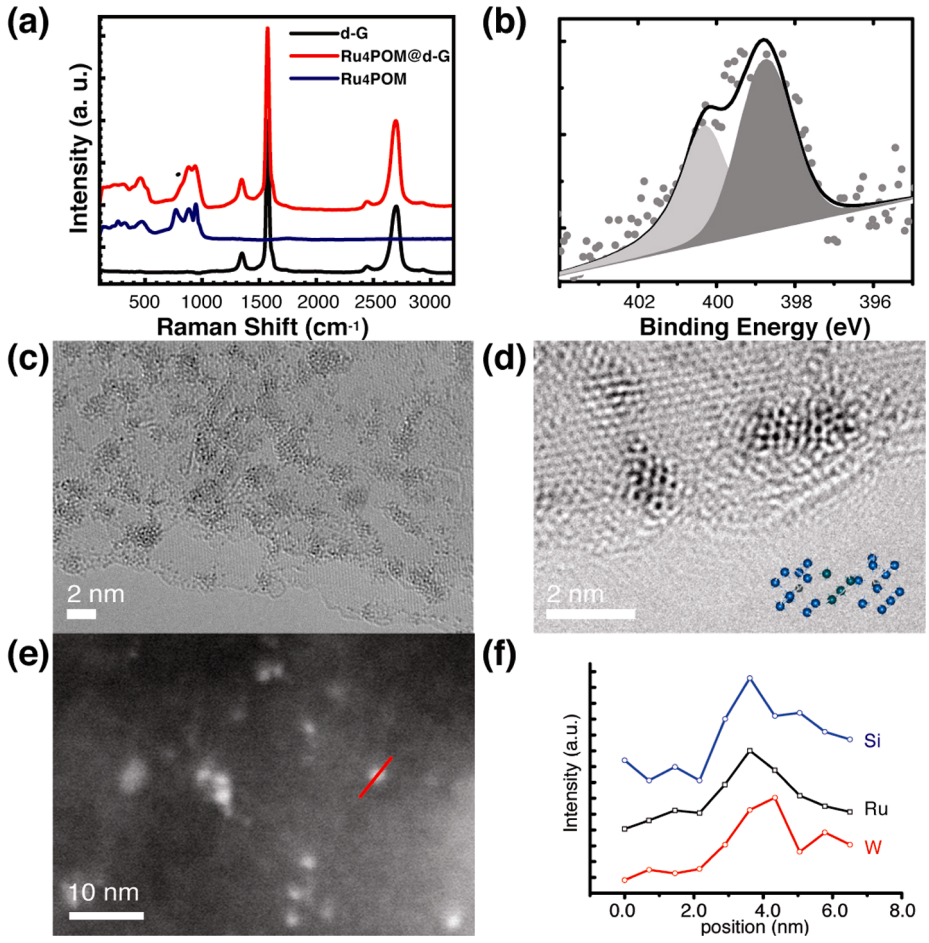

Figure 1. Characterization of Ru_4POM@d-G. (a) Raman spectra of d-G (black curve), Ru_4POM@d-G (red curve), and Ru_4POM (blue curve); (b) XPS spectrum showing N 1s of Ru_4POM@d-G. Imaging of Ru_4POM@d-G (c) AC-TEM acquired at 80 kV (d) HRTEM and Ru_4POM model showing Ru, W, and Si atoms. (e) HAADF-STEM. (f) STEM-EDX line scan across an individual Ru_4POM bright domain, step size of 6.5 Å, and distribution of Si, Ru, and W along the scanned direction, with shifted *y*-scale for clarity reasons.

can be readily modified with regio-selective control, by the orthogonal functionalization of multiple edge/surface sites.[23,24] Additional benefits include a superior chemical inertness, physical robustness as well as adjustable transparency, and optical features[17−22] that are key factors in the implementation of photodevices.

We present herein, the molecular engineering of an unprecedented WOC texture (Figure 1), based on functionalized graphene nanosheets, to integrate the tetra-ruthenium polyoxometalate $\{Ru_4(\mu\text{-}O)_4(\mu\text{−}OH)_2(H_2O)_4[\gamma\text{-}SiW_{10}O_{36}]_2\}^{10-}$ (**Ru_4POM**).[25,26] This latter is the inorganic mimic of the natural photosynthetic Mn_4 cluster. As a multielectron WOC, the **Ru_4POM** possesses a special combination of structural and electronic features:[9] (i) a diamond arrangement with four, oxo-bridged, redox metals, as in the natural enzyme;[25,26] (ii) a rigid, totally inorganic ligand set, with exceptional robustness;[25,26] (iii) a thermodynamic stairway of high valent Ru-intermediates with a redox-potential leveling effect,[27,28] (iv) the highest electron transfer rates ever observed in photocatalytic cycles under artificial environment, in the micro-to-nanoseconds time-range, thus approaching the natural system behavior.[29,30]

In the resulting hybrid material, graphene flat confinement zones are shaped to host the inorganic WOC domains, thereby modulating the electron transfer kinetics through a multilayer morphology, and setting the highest specific surface area potentially available.[17−22,31] This is expected to improve the material wettability and gas-permeation/storage properties thus facilitating the oxygen evolution reaction (OER).[17−22]

Our results confirm a definite upgrade of the electrocatalytic performance mediated by the nanographene environment, when compared to carbon nanotubes with similar surface modification. Most noticeably, the graphene texture is also favoring an exceptional long-term electrode stability, as demonstrated by a reiterated 4 h testing.

RESULTS AND DISCUSSION

Electroactive graphene-based hybrids have been widely obtained from reduced graphene oxide, (**r-GO**).[32,33] Chemical reduction of GO composites is mandatory, to partially restore the sp^2 connectivity and conductivity. However, this treatment produces

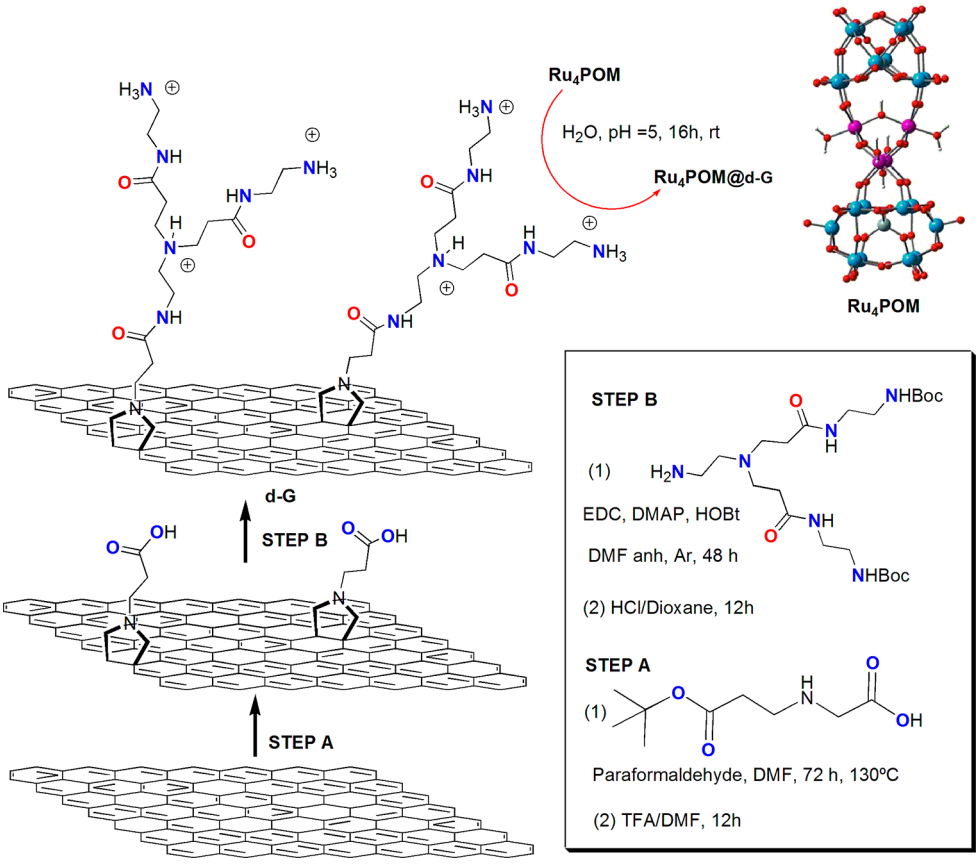

Scheme 1. Synthesis of graphene nano-platform supporting Ru_4POM. Reagents and conditions: Step A: (1) paraformaldehyde, *N,N*-dimethylformamide (DMF), 72 h, 130 °C; (2) trifluoroacetic acid/*N,N*-dimethylformamide, 12 h, room temperature. Step B: (1) dendron d, *N*-(3-dimethylaminopropyl)-*N'*-ethylcarbodiimide, 4-(dimethylamino)pyridine, 1-hydroxybenzotriazole, anhydrous *N,N*-dimethylformamide, 48 h, room temperature, inert atmosphere.

an ill-defined distribution of defects with a high degree of disorder, thus affecting reproducibility.[32,33] Our choice was to preserve the sp^2 carbon network at a larger extent, so we processed pristine graphene (**p-G**), *via* direct 1,3-dipolar cyclo-addition, following a two-step protocol to anchor a first generation polyaminoamide (PAMAM) dendron (Scheme 1).[23,24,34,35] Dendron functionalized graphene (**d-G**) is thus obtained with grafted tertiary and primary branching amino groups, estimated by Kaiser Test analysis to be as high as 0.620 mmol/g. Direct evidence for the successful chemical route **p-G** → **d-G** results from Raman and XPS spectra, in agreement with literature data (Supporting Information, Figure S1, Figure S2, Table S1).[23,24]

The **d-G** platform is designed to host the polyanionic **Ru_4POM** catalyst *via* a cooperative interplay of electrostatic forces and hydrogen bonds. This strategy exploits the complementary charge attraction between the positive ammonium groups formed upon protonation of the terminal dendrimeric anchors on **d-G**, and the negative polyoxometalate residues.[13,14,36] Moreover, the metal-oxo framework of **Ru_4POM** serves as multisite H bond-acceptor, thus reinforcing the supramolecular interaction with the RNH_3^+ functionalized graphene environment.[36] The final outcome is the straightforward scavenging of **Ru_4POM** by **d-G**, performed *via* ion metathesis in aqueous solution at pH = 5 (Scheme 1, see Supporting Information).[13,14]

The resulting material (**Ru_4POM@d-G**) is recovered upon filtration, thoroughly washed with acidic water, and characterized by spectroscopic and electron microscopy techniques, including Raman scattering, XPS, high resolution transmission electron microscopy (HRTEM), scanning electron microscopy (SEM), scanning transmission electron microscopy coupled with energy dispersive X-ray spectroscopy (STEM-EDX). According to Raman evidence, the D band height is preserved in the assembly **Ru_4POM@d-G**, indicating a minor impact of the noncovalent interaction on the material morphology (Figure 1a, red curve), while showing the expected features of molecular **Ru_4POM** (blue curve). Indeed, the Ru-(H_2O) stretching modes are clearly recognized at 250−400 cm^{-1}, together with the tetraruthenate core vibrations at 450−500 cm^{-1}, thus suggesting that the WOC structure is maintained on **d-G** (black curve).[27] XPS data are now implemented by the typical spin−orbit doublet of W 4f, centered at 35.4 eV, and generated by photoelectrons emitted from the W(VI) atoms of the inorganic domains (Supporting Information, Figure S3).[13] Interestingly,

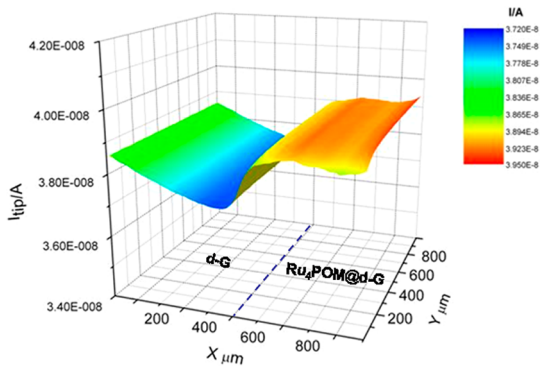

Figure 2. 3D plot of Ru_4POM@d-G catalytic area. SECM mapping of oxygen evolution at the μ-Clark tip on d-G and Ru_4POM@d-G deposited on a glass slide in the presence of 1 mM H_2O_2 (tip potential: −0.7 V referred to Ag/AgCl internal QRE, phosphate buffered saline (PBS) solution).

the hybrid material spectrum shows the N 1s peak with a pronounced reduction of the ammonium component (400.6 eV) as expected due to the preferential interaction with the polyoxometalate domains (Figure 1b).

Imaging of **Ru_4POM@d-G** by aberration-corrected transmission electron microscopy (AC-TEM) allows the inspection of the inorganic cluster distribution (dark contrast, Figure 1c). HRTEM image shown in Figure 1d provides a key evidence of the **Ru_4POM** structure on **d-G**, with atomic resolution and approximately 1 × 2 nm size (see the molecular modeling of one selected projection, inset of Figure 2d). Moreover, the heavy metal domains in **Ru_4POM** are clearly presented as high intensity spots (approximately proportional to the square of the atomic number Z^2) by high-angle annular dark field scanning transmission electron microscopy (HAADF-STEM) shown in Figure 1e. The results of a 10 point STEM-EDX line scan through one individual molecular domain ascribed to the polyoxometalate (line indicated in Figure 1e), confirm the expected spatial distribution of Ru, W, and Si elements (Figure 1f). Noticeably, the EDX signature is retained on both sides of the 2-D graphitic flake, which indicates a double-face amplification of the functional surface (Supporting Information, Figure S4).

Ru_4POM@d-G films have been deposited by solution drop-casting on glass slides, indium tin oxide (ITO) surfaces, and carbon-based screen printed microelectrodes (SPE). SEM images of the hybrid films show a multilayer arrangement, about 40 nm thick, of transparent and slightly corrugated sheets (Supporting Information, Figure S5). These films retain the expected oxygenic evolution activity, inducing a rapid decomposition of added H_2O_2 (1 mM).[37]

Examination of the **Ru_4POM@d-G** material with respect to the catalyst-free **d-G** is obtained by casting both films in contiguity, on the same glass slide (Figure 2). The mapping of the **Ru_4POM** distribution is readily obtained upon addition of aqueous H_2O_2, by a scanning electrochemical microscope (SECM),

TABLE 1. Electrocatalytic Water Oxidation by Ru_4POM Anchored on Functionalized Carbon Nanostructures

@[a]	η (V)[b]	Tafel slope (mVdec^{-1})[c]	TOF_0 (h^{-1})[d]	TOF_{max} (h^{-1})[e]
	0.64	280	0.18	173
MWCNT	0.35	296	0.70	454
d-G	0.30	222	1.73	940

[a] Functionalized carbon nanostructures used as support for anode fabrication. [b] Overpotential of water discharge in 0.2 M aqueous phosphate buffer (pH = 7), determined at an anodic current density value of 150 μA cm^{-2} (data uncorrected for the ohmic drop). [c] mV decade^{-1} determined in the potential range 0.70−1.50 V [*vs* KCl(3M)/AgCl/Ag]. [d] Determined by extrapolation at η = 0 V. [e] Determined at η = 0.6 V.

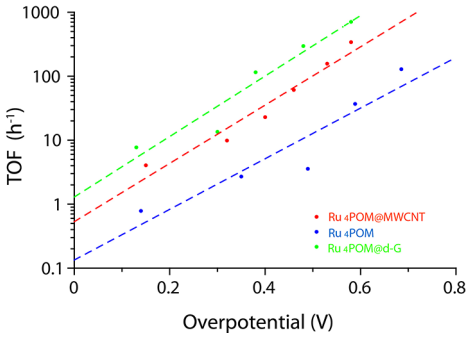

Figure 3. Turn over frequencies as a function of the overpotential of WOC anode. TOF *vs* η Tafel lines for Ru_4POM@d-G (green dots), Ru_4POM (blue dots), and Ru_4@MWCNT (red dots) for the oxygen evolution reaction taking place at dropcast films deposited on carbon-SPE (0.2 M aqueous phosphate buffer, pH = 7). Data are corrected for the ohmic drop.

equipped with a micrometer-sized Clark (μ-Clark) electrode probe with the Pt active part positioned at <100 μm from the hybrid film. The 3D rendering of the μ-Clark electrode response on oxygen evolution displays the contour plot of the catalytically active surface (Figure 2 red-yellow region) with respect to the blank control (blue-green region). This observation confirms both the catalyst coverage and the material wettability.

The WOC performance of **Ru_4POM@d-G** has been evaluated under electrocatalytic conditions with cyclic voltammetry (CV) and chronoamperometry on SPE. These electrodes offer a rapid multitesting protocol and a tailored carbon coating for an ideal adhesion of the nanostructured film. The onset of the catalytic current has been attributed to oxygen evolution, and probed by SECM-μ-Clark electrode.

Comparison with the previously reported MWCNT material, and with the **Ru_4POM** alone can be addressed considering the following descriptors (Table 1): (i) overpotential of water discharge (pH = 7); (ii) Tafel slope; (iii) extrapolated turnover frequency at zero overpotential (TOF_0).[38]

While the similar Tafel slope is indicative of a coherent electrocatalytic mechanism occurring on the diverse electrodic surfaces, and dictated by the **Ru_4POM** multielectronic processes, the overpotential of water oxidation turns out to be lower on the nanographene

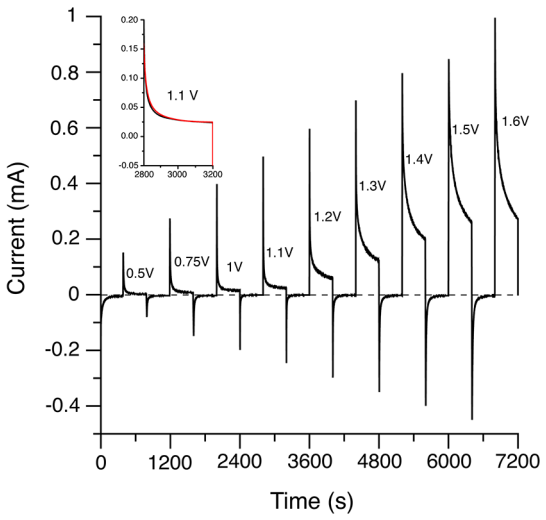

Figure 4. Chronoamperometry of Ru_4POM@d-G. Chronoamperometric current measured at Ru_4POM@d-G carbon-SPE (0.2 M aqueous phosphate buffer, pH = 7), with potential steps up to 1.6 V. Inset: Overlap of oxygen evolution current recorded at 1.1 V at t = 0 and (black line) after 4 h testing (red line).

environment (Table 1). This evidence complies with a key requirement for artificial WOCs.

Analysis of the TOF as a function of the applied overpotential is instrumental to assess the catalyst behavior under the turnover regime and to provide a direct estimate of its quality figures (Figure 3). The TOF-η relationship, derived from chronoamperometry experiments (see Supporting Information and Figure 4), shows a well-behaved linear dependence that allows for a straightforward inspection of the TOF_0 intercept value (Figure 3). This parameter provides an optimal descriptor to rank the intrinsic performance of heterogeneous electrocatalysts.[38] In this frame, the nanographene platform outperforms by 1 order of magnitude the catalytic efficiency of the isolated **Ru_4POM**, with a 2-fold enhancement compared to the nanotube analogues. As a final remark, the stability of the **Ru_4POM@d-G** nanomaterial has been verified by a sequence of chronoamperometric experiments. The anodic potential (E_s) applied was stepped back and forth between 0 V and a positive value in the range 0.5−1.6 V (Figure 4), in order to monitor the oxygen evolution current peak. This process was reiterated, leading to a negligible 1% current loss after 4 h testing (inset in Figure 4).

SUMMARY AND CONCLUSIONS

Graphene−polyoxometalate hybrids retain a major interest in the field of functional materials for artificial photosynthesis, vis-à-vis minimization of the applied overpotential, endorsing long-term robustness. A key aspect in this novel approach is the noninvasive and high-scale surface modification of the graphene nanoplatforms, which enables electron transport and accumulation across the extended π-bond network.

EXPERIMENTAL METHODS

Chemicals. All solvents and chemicals were purchased from Aldrich and used without further purification. Graphite was purchased from Bay Carbon, Inc. (SP-1 graphite powder, www.baycarbon.com).

Characterization Techniques. Raman spectra were recorded with an Invia Renishaw microspectrometer (100×) equipped with laser at 532 nm. Samples were recorded from drops of the dispersions of graphene products in dimethylformamide deposited on glass surfaces. Surfaces were left to dry at room temperature.

HRTEM, HAADF-STEM, and STEM-EDX analyses were performed using a FEI Titan 50−80 "cube" microscope equipped with an aberration corrector for both TEM and STEM mode and EDAX EDX detector, operated at 80 kV in order to minimize knock-on damage to the sample. The HRTEM images were recorded with the C_s value tuned to approximately +15 μm and at under focus, yielding dark atomic contrast for the POM molecules. The monochromator was excited to extend the information limit down to approximately 1 Å. HAADF-STEM was performed using a convergence semiangle of 21 mrad.

X-ray photoelectron spectroscopy (XPS) measurements were performed in a VERSAPROBE PHI 5000 from Physical Electronics, equipped with a monochromatic Al Kα X-ray ($h\nu$ = 1486.6 eV) source with a highly focused beam size that can be set from 10 to 300 μm. The beam size used was 100 μm. The energy resolution was 0.6 eV. For the compensation of the built up charge on the sample surface during the measurements, a dual beam charge neutralization composed of an electron gun (~1 eV) and the argon ion gun (≤10 eV) was used. For the XPS analysis the samples were drop cast on conventional TEM grids (200 mesh, copper) and left to dry. The total covering of the grids by the graphene flakes was verified using an optical microscope—the copper signal in the XPS was used to double check the thickness of the deposition. Binding energies were referenced to the Au 4f7/2 core level. Spectral analysis included a Shirley background subtraction and peak separation using mixed Gaussian−Lorentzian functions. The photoemission peak areas of each element, used to estimate the amount of each species on the surface, were normalized by the sensitivity factors of each element tabulated for the spectrometer used.

SEM micrographs were collected by a Zeiss SUPRA 40VP instrument, with an accelerating voltage of 20 kV, upon drop casting of a water dispersion on a silicon plate.

Two different types of working electrodes were used in the electrochemical experiments, that is, either an ITO conducting electrode or a disk screen-printed carbon electrode (carbon-SPE, DROPSENS S.L., Spain, model DS110). Aqueous **d-G** or **Ru_4POM@d-G** (100 μL, 0.50 ± 0.02 mg mL^{-1}) were deposited on the electrodes in small aliquots of 5 μL at 80 °C. Voltammograms and chronoamperometries of the substrate were recorded with a CHI B910 bipotentiostat or a Biologic SP300 potentiostat. All experiments were carried out in a PTFE cell with a 6 mm diameter aperture, and an O-ring is placed on top of the substrates and tightened using two connecting screws. The cell was also equipped with a platinum wire as counter electrode and with an Ag/AgCl (3 M KCl) reference electrode.

Graphene-Ru_4POM Nanohybrids. *Preparation of d-G.* Exfoliated graphene (0.02 mg mL^{-1}) was produced as reported elsewhere.[34,39] In detail, condensation of paraformaldehyde (0.33 mmol, 2 equiv per graphene carbon) with a modified α-amino acid[40] (0.33 mmol, 2 equiv per graphene carbon) was accomplished in the presence of the graphene colloidal dispersion (200 mL, 0.16 mmol), see Supporting Information (Scheme S1). The mixture was stirred at 130 °C for 72 h with successive additions of the reactants every 24 h. The mixture was then

washed by filtration with dimethylformamide until complete removal of the byproducts. The functionalized graphene was dispersed in dimethylformamide (60 mL, 1 min sonication), then TFA (30 mL) was added. The mixture was kept under magnetic stirring overnight at room temperature. The suspension was filtered and the filter washed with dimethylformamide until neutrality.[23,35]

After cycloaddition and deprotection, graphene was condensed with PAMAM dendron **d** to obtain functionalized graphene **d-G**, Supporting Information, Scheme S1. *N*-(3-dimethylaminopropyl)-*N*′-ethylcarbodiimide (1.6 mmol, 10 equiv), 4-(dimethylamino)pyridine (1.6 mmol, 10 equiv), and 1-hydroxybenzotriazole (1.6 mmol, 10 equiv) were added to **d** (0.8 mmol, 5 equiv per graphene carbon atom) in anhydrous dimethylformamide (35 mL). The mixtures were kept under Ar and magnetically stirred for 48 h. The suspension was filtered and washed with dimethylformamide and then methanol. For the cleavage of the Boc protecting groups, the precipitates were dispersed in dioxane (40 mL), and HCl (12 M, 20 mL) was finally added. The dispersions were kept under magnetic stirring overnight at room temperature. The final mixtures were filtered and washed thoroughly with dimethylformamide and methanol. Then, the final precipitate was dispersed in fresh water pH 5 (6 mL). The quantification of the free amino groups present on the dendrons was carried out by the quantitative Kaiser test. **d-G** resulted in average as 0.620 mmol/g of amino groups.

Synthesis and Characterization of Nanohybrid (Ru_4POM@d-G). Straightforward metathesis techniques were adopted in water solution to anchor **Ru_4POM** to the positively charged **d-G** (see Supporting Information, Scheme S2). In all the experiments 5 mL of an aqueous solution of **d-G** with concentration 0.50 $\pm$ 0.02 mg mL^{-1} were mixed with **Ru_4POM** (23 mg) at pH 5. The mixture was stirred overnight and then the material was recovered by filtration on a Millipore system (filter JHWP 0.2 μm). The solid was dispersed in 5 mL of fresh water pH 5. The loading of the **Ru_4POM** molecules deposited on **Ru_4POM@d-G** were calculated by statistical analysis of 5 STEM images of 80 $\times$ 10^{-2} μm^2 corresponding to different areas on the deposited material.

Conflict of Interest: The authors declare no competing financial interest.

Supporting Information Available: Additional schemes of synthesis, Raman and XPS spectra, SEM and TEM images, and details concerning the electrochemical analysis. This material is available free of charge *via* the Internet at http://pubs.acs.org.

Acknowledgment. Financial support from University of Padova (PRAT 2010 CPDA104105/10, Progetto Strategico 2008 HELIOS prot. STPD08RCX), Fondazione Cariparo (Nanomode Progetti di Eccellenza 2010), INSTM, MIUR (PRIN contract No. 2010N3T9M4, FIRB Nanosolar RBAP11C58Y), the European Commission (project NMP4-SL-2012-310651 SACS) and University of Trieste is gratefully acknowledged. X. Ke, and G. Van Tendeloo are grateful to the ERC for the advanced Grant "COUNTATOMS" and project ESMI. We acknowledge the participation in the ESF Cost Action *NanoTP* (MP0901).

REFERENCES AND NOTES

1. *Faraday Discuss.* **2012**, *155*, 1−388; Special Issue on Artificial Photosynthesis.
2. Tran, P. D.; Wong, L. H.; Barber, J.; Loo, J. S. C. Recent Advances in Hybrid Photocatalysts for Solar Fuel Production. *Energy Environ. Sci.* **2012**, *5*, 5902–5918.
3. Umena, Y.; Kawakami, K.; Shen, J.-R.; Kamiya, N. Crystal Structure of Oxygen-Evolving Photosystem II at a Resolution of 1.9 Å. *Nature* **2011**, *473*, 55–60.
4. Gray, H. B. Powering the Planet with Solar Fuel. *Nat. Chem.* **2009**, *1*, 7.
5. Hammarström, L.; Wasielewski, M. R. Biomimetic Approaches to Artificial Photosynthesis. *Energy Environ. Sci.* **2011**, *4*, 2339.
6. Tachibana, Y.; Vayssieres, L.; Durrant, J. R. Artificial Photosynthesis for Solar Water-Splitting. *Nat. Photonics* **2012**, *6*, 511–518.
7. Du, P.; Eisenberg, R. Catalysts Made of Earth-Abundant Elements (Co, Ni, Fe) for Water Splitting: Recent Progress and Future Challenges. *Energy Environ. Sci.* **2012**, *5*, 6012–6021.
8. Dau, H.; Limberg, C.; Reier, T.; Risch, M.; Roggan, S.; Strasser, P. The Mechanism of Water Oxidation: From Electrolysis *via* Homogeneous to Biological Catalysis. *ChemCatChem* **2010**, *2*, 724–761.
9. Sartorel, A.; Carraro, M.; Toma, F. M.; Prato, M.; Bonchio, M. Shaping the Beating Heart of Artificial Photosynthesis: Oxygenic Metal Oxide Nano-clusters. *Energy Environ. Sci.* **2012**, *5*, 5592–5603.
10. Hocking, R. K.; Brimblecombe, R.; Chang, L.-Y.; Singh, A.; Cheah, M. H.; Glover, C.; Casey, W. H.; Spiccia, L. Water-Oxidation Catalysis by Manganese in a Geochemical-like Cycle. *Nat. Chem.* **2011**, *3*, 461–466.
11. Mola, J.; Mas-Marza, E.; Sala, X.; Romero, I.; Rodríguez, M.; Viñas, C.; Parella, T.; Llobet, A. Ru-Hbpp-Based Water-Oxidation Catalysts Anchored on Conducting Solid Supports. *Angew. Chem., Int. Ed.* **2008**, *47*, 5830–5832.
12. deKrafft, K. E.; Wang, C.; Xie, Z.; Su, X.; Hinds, B. J.; Lin, W. Electrochemical Water Oxidation with Carbon-Grafted Iridium Complexes. *ACS Appl. Mater. Interfaces* **2012**, *4*, 608–613.
13. Toma, F. M.; Sartorel, A.; Iurlo, M.; Carraro, M.; Parisse, P.; Maccato, C.; Rapino, S.; Gonzalez, B. R.; Amenitsch, H.; Da Ros, T.; *et al.* Efficient Water Oxidation at Carbon Nanotube−Polyoxometalate Electrocatalytic Interfaces. *Nat. Chem.* **2010**, *2*, 826–831.
14. Toma, F. M.; Sartorel, A.; Iurlo, M.; Carraro, M.; Rapino, S.; Hoober-Burkhardt, L.; Da Ros, T.; Marcaccio, M.; Scorrano, G.; Paolucci, F.; *et al.* Tailored Functionalization of Carbon Nanotubes for Electrocatalytic Water Splitting and Sustainable Energy Applications. *ChemSusChem* **2011**, *4*, 1447–1451.
15. Li, F.; Zhang, B.; Li, X.; Jiang, Y.; Chen, L.; Li, Y.; Sun, L. Highly Efficient Oxidation of Water by a Molecular Catalyst Immobilized on Carbon Nanotubes. *Angew. Chem., Int. Ed.* **2011**, *50*, 12276-12279.
16. Wu, J.; Xue, Y.; Yan, X.; Yan, W.; Cheng, Q.; Xie, Y. Co_3O_4 Nanocrystals on Single-Walled Carbon Nanotubes as a Highly Efficient Oxygen-Evolving Catalyst. *Nano Res.* **2012**, *5*, 521–530.
17. Brownson, D. A. C.; Kampouris, D. K.; Banks, C. E. Graphene Electrochemistry: Fundamental Concepts through to Prominent Applications. *Chem. Soc. Rev.* **2012**, *41*, 6944–6976.
18. Wei, W.; Qu, X. Extraordinary Physical Properties of Functionalized Graphene. *Small* **2012**, *8*, 2138–2151.
19. Luo, B.; Liu, S.; Zhi, L. Chemical Approaches toward Graphene-Based Nanomaterials and Their Applications in Energy-Related Areas. *Small* **2012**, *8*, 630–646.
20. Huang, X.; Qi, X. Y.; Boey, F.; Zhang, H. Graphene-Based Composites. *Chem. Soc. Rev.* **2012**, *41*, 666–686.
21. Xiang, Q. J.; Yu, J. G.; Jaroniec, M. Graphene-Based Semiconductor Photocatalysts. *Chem. Soc. Rev.* **2012**, *41*, 782–796.
22. Sun, Y.; Wu, Q.; Shi, G. Graphene Based New Energy Materials. *En. Env. Sci.* **2011**, *4*, 1113–1132.
23. Quintana, M.; Montellano López, A.; del Rio Castillo, A. E.; van Tendeloo, G.; Bittencourt, C.; Prato, M. Selective Organic Functionalization of Graphene Bulk or Graphene Edges. *Chem. Commun.* **2011**, *47*, 9330–9332.
24. Quintana, M.; Vazquez, E.; Prato, M. Organic Functionalization of Graphene in Dispersions. *Acc. Chem. Res.* **2012**, 10.1021/ar300138e.
25. Sartorel, A.; Carraro, M.; Scorrano, G.; De Zorzi, R.; Geremia, S.; McDaniel, N. D.; Bernhard, S.; Bonchio, M. Polyoxometalate Embedding of a Tetraruthenium(IV)-Oxo-Core by Template-Directed Metalation of $[\gamma\text{-}SiW_{10}O_{36}]^{8-}$: A Totally Inorganic Oxygen-Evolving Catalyst. *J. Am. Chem. Soc.* **2008**, *130*, 5006–5007.
26. Geletii, Y. V.; Botar, B.; Kögerler, P.; Hillesheim, D. A.; Musaev, D. G.; Hill, C. L. An All-Inorganic, Stable, and Highly Active Tetraruthenium Homogeneous Catalyst for Water Oxidation. *Angew. Chem., Int. Ed.* **2008**, *47*, 3896–3899.

27. Sartorel, A.; Miró, P.; Salvadori, E.; Romain, S.; Carraro, M.; Scorrano, G.; Di Valentin, M.; Llobet, A.; Bo, C.; Bonchio, M. Water Oxidation at a Tetraruthenate Core Stabilized by Polyoxometalate Ligands: Experimental and Computational Evidence To Trace the Competent Intermediates. *J. Am. Chem. Soc.* **2009**, *131*, 16051–16053.
28. Geletii, Y. V.; Besson, C.; Hou, Y.; Yin, Q.; Musaev, D. G.; Quiñonero, D.; Cao, R.; Hardcastle, K. I.; Proust, A.; Kögerler, P.; Hill, C. L. Structural, Physicochemical, and Reactivity Properties of an All-Inorganic, Highly Active Tetraruthenium Homogeneous Catalyst for Water Oxidation. *J. Am. Chem. Soc.* **2009**, *131*, 17360–17370.
29. Natali, M.; Orlandi, M.; Berardi, S.; Campagna, S.; Bonchio, M.; Sartorel, A.; Scandola, F. Photoinduced Water Oxidation by a Tetraruthenium Polyoxometalate Catalyst: Ion-Pairing and Primary Processes with $Ru(bpy)_3^{2+}$ Photosensitizer. *Inorg. Chem.* **2012**, *51*, 7324–7331.
30. Orlandi, M.; Argazzi, R.; Sartorel, A.; Carraro, M.; Scorrano, G.; Bonchio, M.; Scandola, F. Ruthenium Polyoxometalate Water Splitting Catalyst: Very Fast Hole Scavenging from Photogenerated Oxidants. *Chem. Commun.* **2010**, *46*, 3152–3154.
31. Güell, A. G.; Ebejer, N.; Snowden, M. E.; Macpherson, J. V.; Unwin, P. R. Structural Correlations in Heterogeneous Electron Transfer at Monolayer and Multilayer Graphene Electrodes. *J. Am. Chem. Soc.* **2012**, *134*, 7258–7261.
32. Chen, D.; Feng, H.; Li, J. Graphene Oxide: Preparation, Functionalization, and Electrochemical Applications. *Chem. Rev.* **2012**, *112*, 6027–6053.
33. Loh, K. P.; Bao, Q.; Eda, G.; Chhowalla, M. Graphene Oxide as a Chemically Tunable Platform for Optical Applications. *Nat. Chem.* **2010**, *2*, 1015–1024.
34. Quintana, M.; Spyrou, K.; Grzelczak, M.; Browne, W. R.; Rudolf, P.; Prato, M. Functionalization of Graphene *via* 1,3-Dipolar Cycloaddition. *ACS Nano* **2010**, *4*, 3527–3533.
35. Montellano López, A.; Scarel, F.; Rubio Carrero, N.; Vázquez, E.; Mateo-Alonso, A.; Da Ros, T.; Prato, M. Synthesis and Characterization of Highly Water-Soluble Dendrofulleropyrrolidine Bisadducts with DNA Binding Activity. *Org. Lett.* **2012**, *14*, 4450–4453.
36. Carraro, M.; Sartorel, A.; Scorrano, G.; Maccato, C.; Dickman, M. H.; Kortz, U.; Bonchio, M. Chiral Strandberg-Type Molybdates $[(RPO_3)_2Mo_5O_{15}]^{2-}$ as Molecular Gelators: Self-Assembled Fibrillar Nanostructures with Enhanced Optical Activity. *Angew. Chem., Int. Ed.* **2008**, *47*, 7275–7279.
37. Sartorel, A.; Truccolo, M.; Berardi, S.; Gardan, M.; Carraro, M.; Toma, F. M.; Scorrano, G.; Prato, M.; Bonchio, M. Oxygenic Polyoxometalates: A New Class of Molecular Propellers. *Chem. Commun.* **2011**, *47*, 1716–1718.
38. Costentin, C.; Drouet, S.; Rebert, M.; Savéant, J.-M. Turnover Numbers, Turnover Frequencies, and Overpotential in Molecular Catalysis of Electrochemical Reactions. Cyclic Voltammetry and Preparative-Scale Electrolysis. *J. Am. Chem. Soc.* **2012**, *134*, 11235–11242.
39. Hernandez, Y.; Nicolosi, V.; Lotya, M.; Blighe, F. M.; Sun, Z.; De, S.; McGovern, I. T.; Holland, B.; Byrne, M.; Gun'Ko, Y. K.; *et al.* High-Yield Production of Graphene by Liquid-Phase Exfoliation of Graphite. *Nat. Nanotechnol.* **2008**, *3*, 563–568.
40. Milic, D.; Prato, M. Fullerene Unsymmetrical Bis-adducts as Models for Novel Peptidomimetics. *Eur. J. Org. Chem.* **2010**, *3*, 476–483.